Small Signal Modeling and Control Loop Design of Critical Conduction Mode Active Clamp Flyback Converter

Shengyou Xu, *Student Member, IEEE*, Qinsong Qian, Tao Tao, Shengli Lu, and Weifeng Sun, *Senior Member, IEEE*

***Abstract*—Critical conduction mode (CrCM) active clamp flyback (ACF) converter is regarded as a good candidate to be applied in high-frequency small power supplies. This article focuses on the modeling, analysis, and controller design of CrCM-ACF converter. The small signal model of the converter is derived based on a zero-input resonant equivalent circuit and extended describing function (EDF) method for the first time, then the obtained full-order model is simplified to a low-order model. This procedure establishes an insightful understanding about the effects of the converter parameters and working conditions. Based on the simplified model, a control loop compensator is designed in a single-loop voltage-feedback control scheme for high dynamic performance. An experimental prototype of digital controlled CrCM-ACF converter is built, the accuracy of the derived model is verified by comparing with experimental and simulation results. The performance of the compensator is experimentally evaluated by applying abrupt load current and reference voltage changes in the operating conditions of the converter. From the experimental results, it is demonstrated that the derived analytical model and designed compensator are effective in regulating the output voltage in CrCM-ACF converter.**

***Index Terms*—Active clamp flyback (ACF) converter, continuous conduction mode (CCM), controller design, critical conduction mode (CrCM), extended describing function (EDF) modeling.**

I. Introduction

THE rapid development of power electronics results in the optimization of power adapters are developed toward smaller size, higher power density, and higher efficiency. It is effective to decrease the size and improve the power density by increasing switching frequency, but it increases the power loss of the widely used hard switching flyback converter in small power supplies [1], [2]. By adding a clamp capacitor and a clamp power switch in flyback, active clamp flyback (ACF) converter has a smaller voltage stress and a higher efficiency since the zero voltage switching (ZVS) of primary power switches can be realized [3]. Therefore, ACF is regarded as a good candidate to be used in small size high-frequency adapters.

According to different working status, ACF has two modes, continuous conduction mode (CCM) [4], [5] and critical conduction mode (CrCM) [6], [7] (hereafter referred as "CCM-ACF" and "CrCM-ACF," respectively). Due to the different operating characteristic, CCM-ACF is more similar to a pulsewidth modulation (PWM) converter rather than a resonant converter, CrCM-ACF is a half-PWM half-resonant converter. It was demonstrated that CrCM-ACF is better than CCM-ACF in the aspects of ZVS range, EMI problems and the zero current switch-OFF (ZCS) ability of output rectifier in high-frequency applications [8]. Therefore, CrCM-ACF has been implemented in many high-frequency prototypes [9], [10]. However, since the distinctive asymmetric half-PWM half-resonant operating characteristic, the accurate small signal model of CrCM-ACF converter has not been presented. Hence, the designed controller in the prototype is usually by cut-and-trial method, which increases the design time and is disadvantageous for the performance prediction of the system. Therefore, this article focus on the accurate small signal modeling and control-loop compensator design of CrCM-ACF converter. The main operating process and performance comparison between CCM and CrCM ACF converter will be illustrated in details in the following section.

The conventional state space averaging method (SSA) has been popularly used to model many PWM converters [11]–[13], as well as ACF converter [14]. However, SSA only can be used to model CCM-ACF rather than CrCM-ACF owing to the resonant performance of CrCM-ACF cannot be reflected by the linearized and averaged modeling principle. The phase plane [15]–[16] and signal flow graph [17]–[18] are two graphic modeling methods, which are intuitive and easy to analysis. However, their modeling principle are also based on SSA, so the accurate small signal model of CrCM-ACF converter still cannot be derived by these two methods. The sampled-data or discrete-time [19], [20] approach is effective to capture the inherent sampling nature and predict the small signal characteristic in resonant converters. However, only the numerical solution of the small signal model can be derived at specific operating conditions, which makes the designed compensator is a big challenge and becomes unmanageable if the operation of the converter

Manuscript received June 20, 2020; revised September 20, 2020 and October 19, 2020; accepted November 16, 2020. Date of publication November 25, 2020; date of current version February 5, 2021. This work was supported in part by the Key Research and Development Plan of Jiangsu under Grant BE2018003-3, and in part by the National Key Research and Development Plan under Grant 2017YFB0402900. Recommended for publication by Associate Editor B. Singh. *(Corresponding author: Qinsong Qian.)*

The authors are with the National ASIC System Engineering & Research Center, Southeast University, Nanjing 211189, China (e-mail: xsyjoy@foxmail.com; qianqinsong@seu.edu.cn; xxixv19951031@qq.com; lsl@seu.edu.cn; swffrog@seu.edu.cn).

Color versions of one or more of the figures in this article are available online at https://ieeexplore.ieee.org.

Digital Object Identifier 10.1109/TPEL.2020.3040451

involves different modes. In addition, the computational process of modeling procedure is too complex for practical use [21]. This article utilizes the extended describing function (EDF) method to derive the small signal model of CrCM-ACF converter. EDF is a systematic approach to developing the small signal model to investigate the stability characteristic for different control status, and which is widely used in resonant converts [22]–[26]. The advantage of implementing EDF as the modeling method is that the resonant performance of CrCM-ACF can be fully expressed. This advantage results in an excellent performance of the behavior and response of the converter in steady and transient state.

In EDF modeling procedure, each of the state variables has a sinusoidal waveform. However, the unsymmetrical half-PWM half-resonant operating process results in the state variables of CrCM-ACF are not varied sinusoidally, so which limits the application of EDF in CrCM-ACF converter [27]. Therefore, a zero-input resonant equivalent circuit is proposed for the first time, and then the accurate small signal model of CrCM-ACF converter is derived by EDF method. Based on the derived model, the frequency characteristic is analyzed, and control loop compensator in a single-loop voltage-feedback control system is designed. The contributions of this article may be summarized as follows.

1) The proposed zero-input resonant equivalent circuit integrate the PWM and resonant operating processes, transfer the asymmetry half-PWM half-resonant mode to a pure resonant process, which provides a new modeling idea for the active clamp converter.
2) The comparison among the derived model, the simulation and experimental results show the obtained model can be accurate up to the half of switching frequency. The simplified model has a very clear zero-pole style, which is very beneficial for the frequency characteristic analysis and controller design in CrCM-ACF converter.
3) The designed high-frequency compensator in a single-loop, voltage-feedback control system, which is better that the widely used PI or PID controller. This procedure presents a clear controller design step, which is beneficial for the application of CrCM-ACF converter.
4) The detailed studies and experiment based on the derived model and designed controller are presented. The stability performance investigation leads to the conclusion that the designed controller has the ability to predict the steady state and dynamic responses of the converter.

The rest of this article is organized as follows. In Section II, the main operating processes and characteristics between CCM and CrCM ACF converter are compared and analyzed in details. Then, the SSA average model of CCM and CrCM ACF converter are compared with simulation results, respectively. In Section III, a zero-input resonant equivalent circuit is proposed according to the operating behavior of CrCM-ACF converter. Afterward, the corresponding small signal model is derived based on EDF modeling method. In order to use the small signal model in control loop, the obtained high order model is simplified and analyzed. In Section IV, based on the obtained control-to-output transfer function, a high-performance control loop compensator is designed for CrCM-ACF converter. In Section V, a CrCM-ACF prototype is designed to verify the derived small signal model and implement the designed compensator. Finally, Section VI concludes this article.

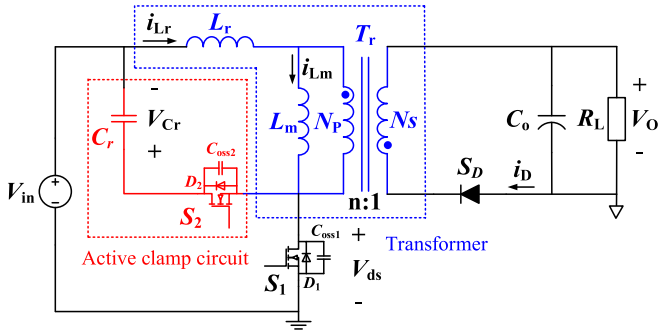

Fig. 1. Topology of ACF converter.

II. Comparison Between CCM and CrCM ACF Converter

A. Operating Characteristic Comparison

The topology of ACF converter is shown in Fig. 1. S_1 and S_2 are the primary main and clamp power switch, respectively. $C_{\rm oss1}$ and $C_{\rm oss2}$ are the parasitic capacitor of S_1 and S_2 respectively, D_1 and D_2 are the parasitic body diode of S_1 and S_2, respectively. Moreover, L_m and L_r are the magnetizing and leakage inductor, respectively, and are usually integrated in the transformer of ACF converter. C_r and C_o are the clamp and output capacitor, respectively. S_D is the secondary rectifier, R_L is the load resistor, and n is the turn ratio of the transformer. In addition, $V_{\rm in}$ and V_o represent the input and output voltage, respectively.

The key waveforms of CCM and CrCM ACF converter are shown in Fig. 2(a) and (b), respectively. $V_{\rm gs}$ is the gate signals of S_1 and S_2. $i_{\rm Lr}$ and $i_{\rm Lm}$ are the resonant and magnetizing current, respectively. $V_{\rm ds}$ is the voltage between the drain and source of S_1, and $V_{\rm Cr}$ is the voltage across C_r. i_D is the current through S_D. I_v is the minimum magnetizing current. $T_{\rm d1}$ is the dead time between the turn-OFF moment of S_1 and the turn-ON moment of S_2. $T_{\rm d2}$ is the dead time between the turn-OFF moment of S_2 and the turn-ON moment of S_1. T_s is the switching period, and D is the turn ratio.

In CCM-ACF converter, there are three main operation modes from $t = t_{\rm a0}$ to $t = t_{\rm a6}$. The first one is energy storage mode ($M_{\rm a1}$) from $t = t_{\rm a1}$ to $t = t_{\rm a2}$. During this mode, the energy stored in L_m and L_r are charged by $V_{\rm in}$, so $i_{\rm Lr}$ and $i_{\rm Lm}$ are increased linearly. Since the energy cannot be transferred from primary to secondary, V_o is stabled by C_o. The equivalent circuit of mode $M_{\rm a1}$ is shown in Fig. 3(a).

The second one is energy transfer mode ($M_{\rm a2}$) from $t = t_{\rm a3}$ to $t = t_{\rm a4}$. During this time interval, the energy can be delivered from primary to secondary, the voltage across L_m is clamped by V_o. L_r resonant with C_r. The equivalent circuit of mode $M_{\rm a2}$ is shown in Fig. 3(b).

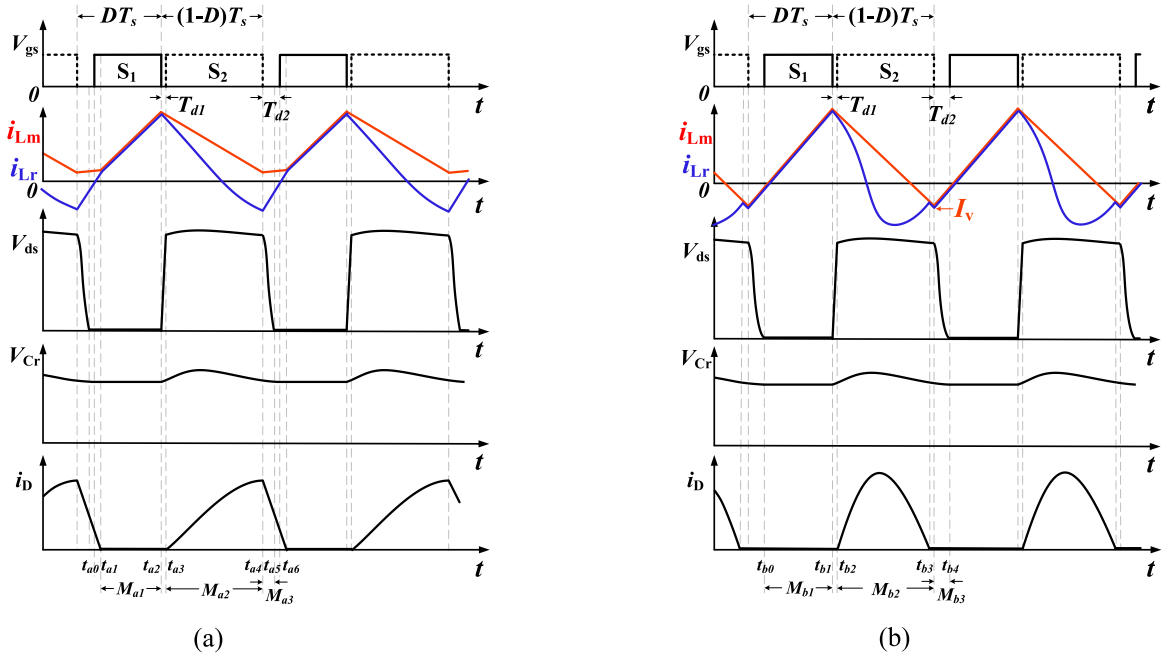

Fig. 2. Key waveforms of (a) CCM and (b) CrCM ACF converters.

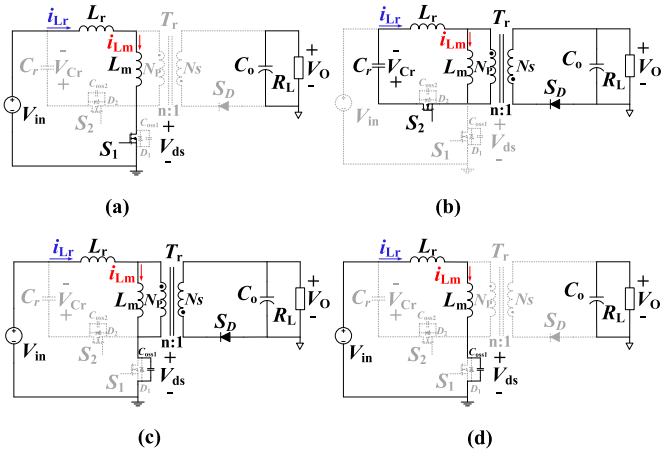

Fig. 3. Main equivalent circuits of ACF converter. (a) Ma1 or Mb1. (b) Ma2 or Mb2. (c) Ma3. (d) Mb3.

The third one is ZVS realization mode (M_{a3}) from $t = t_{a4}$ to $t = t_{a5}$ in T_{d2}. Although the energy also can be transferred from primary to secondary, the main purpose of this mode is to realize the ZVS of S_1. When S_2 turn-OFF, the resonant object of L_r is changed from C_r to C_{oss1}. Then, V_{ds} is decreased and the ZVS of S_1 can be reached. The equivalent circuit of mode M_{a3} is shown in Fig. 3(c).

The same as CCM-ACF converter, there are also three similar main operation modes from $t = t_{b0}$ to $t = t_{b4}$ in CrCM-ACF converter. The energy storage mode M_{b1} is from $t = t_{b0}$ to $t = t_{b1}$, which has an identical operation process to M_{a1}. The energy transfer mode M_{b2} which is from $t = t_{b2}$ to $t = t_{b3}$ also has a similar operation process to M_{a2}. However, the difference of them is that, the resonant deepness of the resonance process between L_r and C_r in M_{b2} is more thorough than M_{a2}. Therefore, unlike the energy in M_{a2} that cannot be wholly transferred from primary to secondary, the energy can be fully delivered in M_{b2}. Since the energy which used to actualize the ZVS of S_1 in CrCM-ACF is disparate with CCM-ACF converter, the ZVS realization mode M_{b3} from $t = t_{b3}$ to $t = t_{b4}$ is different to M_{a3}. The energy applies to realize ZVS is stored in L_r in CCM-ACF, while that is mainly stored in L_m in CrCM-ACF converter. Therefore, in M_{b3}, L_m also join into the resonance process with L_r and C_{oss1}, to realize the ZVS of S_1. The equivalent circuit of modes M_{b1} and M_{b2} are similar to M_{a1} and M_{a2}, respectively. The equivalent circuit of mode M_{b3} is shown in Fig. 3(d). The detailed operation processes of CCM and CrCM ACF converter can refer to [4], [5] and [6], [7], respectively.

By comparing with the operation processes, it can be seen that the main difference between CCM and CrCM ACF converter is the ZVS realization mode. In CCM-ACF converter, the energy used to realize the ZVS of S_1 in M_{a3} is stored in L_r, so an incomplete resonant current i_{Lr} waveform in M_{a2} is needed to provide the initial ZVS energy at the turning point $t = t_{a4}$. However, this ZVS energy reduces with load decreases. At light load current, ZVS may lost, then resulting in a poor efficiency [28]. An additional inductor is usually required to store enough energy for full ZVS, but it also increases the size of the system. Although increasing switching frequency can reduce the size effectively, it aggravates the ZVS performance of CCM-ACF converter. Moreover, the ZCS of S_D cannot be reached, which may generate voltage oscillations and noises. Due to these limitations, CCM-ACF is not suitable for small size high-frequency applications.

Unlike CCM-ACF converter, i_{Lm} is reversed to negative during every switching cycle to make ZVS come true in CrCM-ACF converter. By controlling the minimum negative magnetizing

current I_v, the ZVS of S_1 can be completely realized in M_{a3} no matter what operating condition is [28]. In addition, because the ZVS do not relies on i_{Lr}, the operation mode M_{b2} can be designed to have an absolute resonance process between L_r and C_r, and then the ZCS of S_D can be achieved at the turn-OFF instant. Therefore, CrCM-ACF can be switched efficiently and cleanly, and which has a higher performance than CCM-ACF converter in high-frequency systems.

Different operation processes perform different waveforms, and then give expression to different characteristics. Therefore, the linearly changed current waveform exhibits a PWM performance, while the sinusoidally changed current waveform expresses a resonant performance. Since the linearly and sinusoidally varied current waveforms coexist in one switching cycle, CrCM-ACF converter has a synthetical performance of PWM and resonant converter. Hence, CrCM-ACF is a half-PWM half-resonant converter. On the contrary, although the resonance processes also exist, CCM-ACF converter is more similar to a PWM converter rather than a resonant converter. Therefore, the small signal model, which can reflect the frequency characteristic of CrCM-ACF converter, would be different from CCM-ACF converter.

B. Average Model Comparison

SSA modeling method is widely used for control loop analysis and compensator design in many converters. The small signal model of ACF converter, which is derived by SSA, has also been presented in [14]. The relative analytical model of control-to-output transfer function is given as (1), shown at the bottom of this page.

SIMPLIS simulation software is popularly and effectively applied in small signal verification [29]. The Frequency response comparison between SIMPLIS simulation results and SSA average models of CCM-ACF and CrCM-ACF converter are shown in Figs. 4 and 5, respectively. From these two figures, it can be seen that, the frequency response curves of the average model are highly agreement with the simulation result in CCM-ACF converter, while which is hardly in agreement with the simulation result in CrCM-ACF converter. The reason is that the resonance processes and characteristic of CrCM-ACF converter cannot be reflected by SSA model.

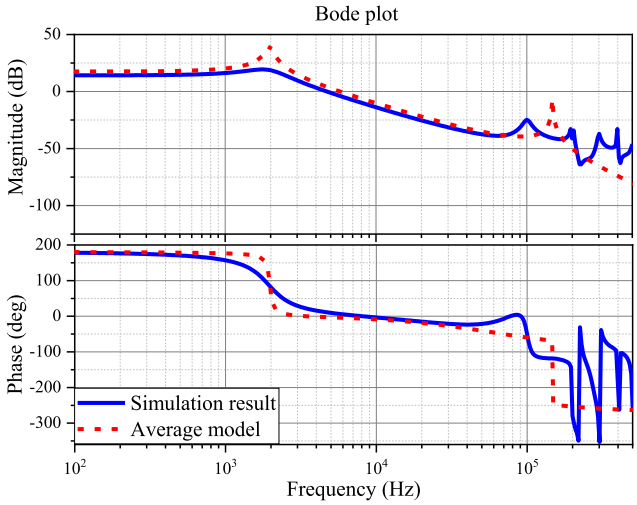

Fig. 4. Frequency response comparison between simulation result and average model in CCM-ACF converter.

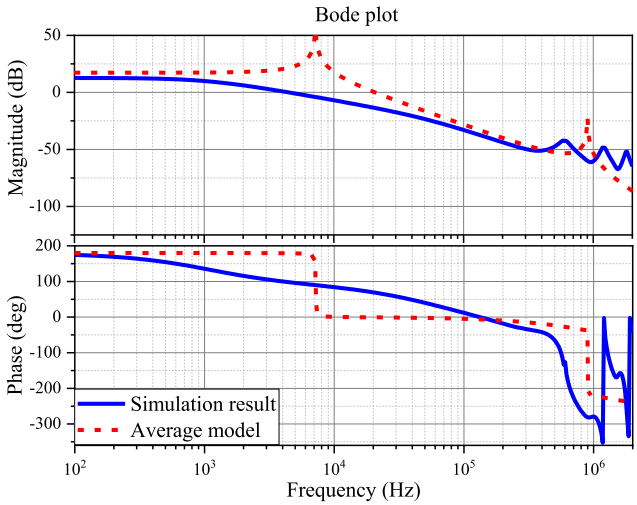

Fig. 5. Frequency response comparison between simulation result and average model in CrCM-ACF converter.

III. Small Signal Model of CrCM-ACF Converter

Using EDF modeling method, the resonance processes in resonant converter are embodied completely. Therefore, in order to include and express the resonance performance of CrCM-ACF converter, the accurate small signal model of CrCM-ACF also should be derived by EDF method. However, the needed nonlinear differential equation group [26] in CrCM-ACF converter cannot be obtained directly owing to the half-PWM half-resonant operating principle. Therefore, a zero-input resonant equivalent circuit is proposed to derive the nonlinear differential equations first, and then the accurate small signal model is derived by EDF method.

A. Zero-Input Resonant Equivalent Circuit

According to the operating characteristic of CrCM-ACF converter, when it works in M_{b1}, the energy is mostly stored in L_m, and which is not transferred to the output side. Only when it operates in M_{b2}, the energy is delivered from primary to secondary. Therefore, the only correlation between the two modes is that the initial energy of M_{b2} is determined by M_{b1}. If adding this initial energy into the equivalent circuit of M_{b2}, the

$$G_{\mathrm{vd\_SSA}}(s)=\frac{v_o(s)}{d(s)}=\frac{V_{in}L_m[(DL_mL_rC_r)s^2+(D(1-D)^2L_m)s-R_Ln^2(1-D)^4]}{n(L_m+L_r)[(L_mL_rC_rC_oR_L)s^4+(L_mL_rC_r)s^3+(1-D)^2R_L \cdot(n^2C_r(L_m+L_r)+L_mC_o)s^2+((1-D)^2L_m)s+n^2(1-D)^4R_L]} \quad (1)$$

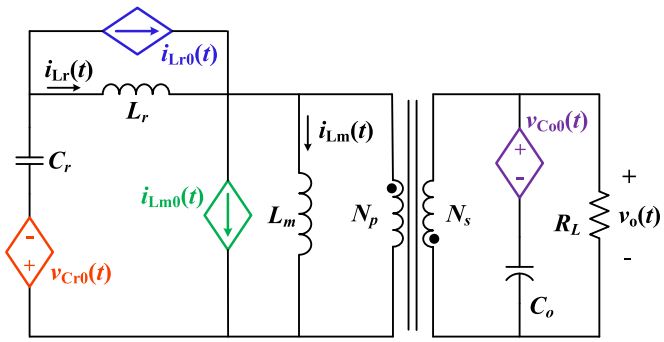

Fig. 6. Zero-input resonant equivalent circuit of CrCM-ACF converter.

two equivalent circuits of M_{b1} and M_{b2} can be integrated and replaced by a zero-input resonant equivalent circuit, as shown in Fig. 6. Furthermore, the half-PWM half-resonant operating process of CrCM-ACF can be fully expressed by this resonant equivalent converter. Then, EDF can be used to derive the ac model of CrCM-ACF converter.

Note that, compared to switching period T_s, the dead time T_{d1} and T_{d2}, which are used to realize the ZVS of S_1 and S_2 respectively, are very small. Therefore, in order to derive the control-to-output transfer function more easily, the operation process in T_{d1} and T_{d2} are ignored, and only the working processes in M_{b1} and M_{b2} are considered.

Compared with the equivalent circuit of M_{b2} in Fig. 3(b), it can be discovered that there are four additional controlled sources in this zero-input resonant equivalent circuit. These controlled sources are used to represent the needed initial energy of M_{b2}. At steady state, the initial energy of M_{b2} is stored in L_m, L_r, C_r, and C_o. Therefore, if the initial energies of L_m, L_r, C_r, and C_o is calculated, the needed initial energy of M_{b2} will be determined.

According to circuit theory, the initial energies of the four passive elements can be represented by their initial voltage or current values, respectively, so which can be obtained if their initial voltage or current values are known. The start of M_{b2} also is the end of M_{b1} if T_{d1} is ignored. Hence, the initial voltage or current values of the four components in M_{b2} can be substituted by the corresponding finish values at the turn-OFF moment $t = t_{b1}$ of M_{b1}, which are given as (2)–(4), respectively

$$i_{Lr0}(t) = i_{Lm0}(t) = \frac{v_{in}(t)}{L_m + L_r}(DT_s - T_{d2}) \tag{2}$$

$$v_{Cr0}(t) = nv_o(t) + \frac{L_r}{L_m + L_r}\frac{D}{1-D}v_{in}(t) \tag{3}$$

$$v_{Co0}(t) = v_o(t) \tag{4}$$

where $i_{Lr0}(t)$ and $i_{Lm0}(t)$ are the initial current value of L_m and L_r in M_{b2}, respectively. $v_{cr0}(t)$ and $v_{co0}(t)$ are the initial voltage value of C_r and C_o in M_{b2}, respectively.

By using the four controlled sources, the initial energy of M_{b2} is reflected by the initial voltage or current values of L_m, L_r, C_r, and C_o. By adding these controlled sources into the equivalent circuit of M_{b2}, the zero-input resonant equivalent circuit is formed to express the resonance characteristic of CrCM-ACF converter. Because of the main part of this zero-input resonant equivalent circuit relies on the resonance process in M_{b2}, the resonant performance of CrCM-ACF converter can be mostly embodied. Meanwhile, since the initial values of the four controlled sources are determined by the PWM process in M_{b1}, the PWM performance of CrCM-ACF converter is also included. Therefore, the half-PWM half-resonant operating performance of CrCM-ACF converter can be completely expressed by this resonant equivalent circuit. Based on it, the needed nonlinear differential equation group can be obtained, and the accurate small signal model of CrCM-ACF converter can be derived by EDF modeling method.

B. EDF Modeling

From this zero-input resonant equivalent circuit, the needed nonlinear differential equation group of CrCM-ACF converter is given as follows:

$$L_m\frac{di_{Lm}(t)}{dt} = nv_o(t)\cdot \mathrm{sgn}\left(\frac{1}{2} - \frac{1}{2}\frac{di_{Lm}(t)}{dt}\right) \tag{5a}$$

$$L_r\frac{di_{Lr}(t)}{dt} = v_{Cr0}(t) + \left(v_{Cr}(t) - L_m\frac{di_{Lm}(t)}{dt}\right) \cdot \mathrm{sgn}\left(\frac{1}{2} - \frac{1}{2}\frac{di_{Lm}(t)}{dt}\right) \tag{5b}$$

$$C_r\frac{dv_{Cr}(t)}{dt} = -i_{Lr0}(t) - i_{Lr}(t)\cdot \mathrm{sgn}\left(\frac{1}{2} - \frac{1}{2}\frac{di_{Lm}(t)}{dt}\right) \tag{5c}$$

$$C_o\frac{dv_{Co}(t)}{dt} = n(i_{Lm}(t) - i_{Lr}(t))\cdot \mathrm{sgn}\left(\frac{1}{2} - \frac{1}{2}\frac{di_{Lm}(t)}{dt}\right) - \frac{v_o(t)}{R_L} + i_o(t) \tag{5d}$$

$$v_o(t) = v_{Co}(t) + v_{Co0}(t). \tag{5e}$$

In EDF modeling procedure, all the state variables are decomposed into their Fourier coefficients. To simplify the EDF modeling procedure, only the fundamental components of the Fourier series of the variables need to be considered, and the higher harmonic components are neglected. Then, the matrix form of the small signal model of CrCM-ACF converter is given as follows:

$$\frac{d\hat{x}}{dt} = A\hat{x} + B\hat{u} + c\hat{y} \tag{6a}$$

$$\hat{y} = D\hat{x} \tag{6b}$$

where

$$\hat{x} = [\hat{i}_{Lms}\ \hat{i}_{Lmc}\ \hat{i}_{Lrs}\ \hat{i}_{Lrc}\ \hat{v}_{Crs}\ \hat{v}_{Crc}\ \hat{v}_{Co}]^T \tag{6c}$$

$$\hat{u} = [\hat{v}_{in}\ \hat{d}\ \hat{w}_s\ \hat{i}_o]^T \tag{6d}$$

$$\hat{y} = [\hat{v}_o]. \tag{6e}$$

All the variables in (6c)–(6e) represent the ac small signal perturbation of the relative variables. By substituting the decomposed state, input and output variables into (5), equaling the

TABLE I
DETAILED PARAMETERS

No.	Name	Symbol	Value
1	Input voltage	V_{in}	120-380Vdc
2	Output voltage	V_o	19.5Vdc
3	Output power	P_o	65W(max)
4	Switching frequency	f_s	0.6-1MHz
5	Clamp capacitor	C_r	8nF
6	Magnetizing inductor	L_m	20uH
7	Leakage inductor	L_r	1uH
8	Output capacitor	C_o	200uF

small signal terms of sin(·), cos(·), and dc components to each other. The calculated state, input and output matrix are shown in (7), as shown at the bottom of this page, where the undetermined parameters are given in the Appendix.

Based on (6) and (7) the transfer function between the output voltage and various control variables can be obtained by using the inverse Laplace transform.

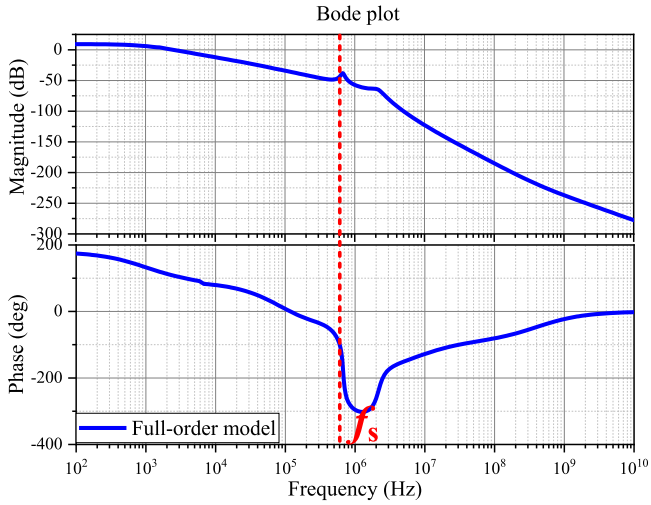

Fig. 7. Frequency response curve of the full order analytical model in CrCM-ACF converter.

C. Model Simplification and Analysis

The detailed circuit parameters in this article are shown in Table I. By using MATLAB, the frequency response curve is shown in Fig. 7. In this figure, $V_{\rm in}$ and V_o are set at 120 and 19.5 V, respectively, f_s is set at 600 kHz. In engineering, it is better to use a low-order model for control loop analysis and compensator design. However, the obtained small signal model is a high-order model due to the state variables are decomposed by the sine and cosine terms of their Fourier series in EDF modeling procedure. Moreover, the needed poles and zeros, which are concealed in the high-order model, are hard to be calculated. Although the numerical solution of theses poles and zeros can be obtained by *zpk* function or plot by *pzmap* function in MATLAB, the influence factor of these poles and zeros still cannot be determined directly.

Fig. 8 shows the pole-zero map by using *pzmap* function. It can be seen that there are six zeros and seven poles exist in the derived high-order analytical model. However, most of them are high-frequency poles and zeros, which are larger than switching frequency and nonsignificant for real applications. Therefore, the gained high-order model is not useful for control loop design, and which need to be simplified by eliminating the non-significant zeros and poles.

According to (6) and (7), the full-order analytical model can be calculated. By simplifying the coefficients in the full-order model and decomposing the simplified coefficients, an idealized control-to-output transfer function, which have a zero-pole form can be obtained. Due to the complicated mathematical computation in the derivation process, the simplified transfer function is directly given as (8)

$$G_{\rm vd\_simp}(s)=\frac{K_g(s-w_z)}{(s+w_{p1})(s+w_{p2})(1+\frac{s}{Q_n w_n}+\frac{s^2}{w_n{}^2})} \tag{8a}$$

$$A=\begin{bmatrix} 0 & \Omega_s & 0 & 0 & 0 & 0 & 0\\ -\Omega_s & 0 & 0 & 0 & 0 & 0 & 0\\ 0 & 0 & 0 & \Omega_s & \frac{1}{L_r} & 0 & 0\\ 0 & 0 & -\Omega_s & 0 & 0 & \frac{1}{L_r} & 0\\ 0 & 0 & -\frac{1}{C_r} & 0 & 0 & \Omega_s & 0\\ 0 & 0 & 0 & -\frac{1}{C_r} & -\Omega_s & 0 & 0\\ \frac{32nD(1-D)k_s}{C_o} & \frac{32nD(1-D)k_c}{C_o} & -\frac{8nL_r(1-D)k_s}{C_rC_o} & -\frac{n(1-D)k_c}{C_o} & 0 & 0 & 0 \end{bmatrix} \tag{7a}$$

$$B=\begin{bmatrix} 0 & 0 & \frac{1}{L_m+L_r}\frac{D^2}{1-D} & \frac{1}{L_m+L_r}\frac{D^2}{1-D} & \frac{D(DT_s-T_m)}{(L_m+L_r)C_r} & \frac{D(DT_s-T_m)}{(L_m+L_r)C_r} & 0\\ \frac{nD^3(1-D)V_o}{12L_m} & \frac{nD^5(1-D)V_o}{4{V_{in}}^3L_mT_s} & \frac{-D^4(D+2)}{4(1-D)(L_m+L_r)} & \frac{-V_{in}D^4(D+2)}{12(1-D)(L_m+L_r)} & \frac{-D^4(1-D)T_s}{2(L_m+L_r)C_r} & \frac{-15D^4(1-D)T_s}{(L_m+L_r)C_r} & \frac{nD^3(1-D)(I_{Lm}-I_{Lr})}{4V_{in}C_o}\\ I_{Lmc} & -I_{Lms} & I_{Lrc} & -I_{Lrs} & V_{Crc} & -V_{Crs} & 0\\ 0 & 0 & 0 & 0 & 0 & 0 & \frac{1}{C_o} \end{bmatrix}^T \tag{7b}$$

$$C=\begin{bmatrix} \frac{nD^2(1-D)^3}{L_m} & \frac{nD^2(1-D)^3}{L_m} & -\frac{nDT_s}{L_r} & -\frac{nDT_s}{L_r} & 0 & 0 & -\frac{1}{R_LC_o} \end{bmatrix}^T \tag{7c}$$

$$D=\begin{bmatrix} 0 & 0 & 0 & 0 & 0 & 0 & 1 \end{bmatrix} \tag{7d}$$

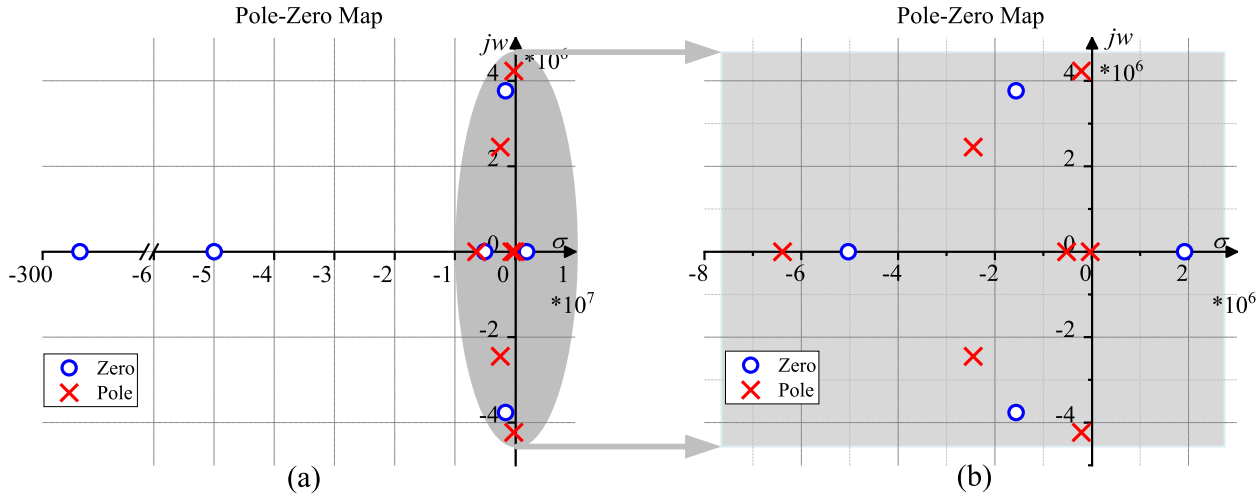

Fig. 8. Pole-zero map of the full order analytical model in CrCM-ACF converter.

where

$$K_g = \frac{21D^4\pi^3 {V_{in}}^3 {f_s}^3 L_r C_r}{2(1-D)} \tag{8b}$$

$$w_z = \frac{4f_s}{5D(1-D)} \tag{8c}$$

$$w_{p1} = D(1-D)L_m(D{\Omega_s}^2 C_o + (1-D)f_s R_L^2) \tag{8d}$$

$$w_{p2} = \frac{D(D-1)^2(2n^2(L_m+L_r)K_c - R_L C_o K_s)}{\Omega_s L_r(C_o L_m - {\Omega_s}^2 L_m L_r C_o C_r)} \tag{8e}$$

$$w_n = \frac{\sqrt{5}}{2}\Omega_s \tag{8f}$$

$$Q_n = \frac{2\sqrt{5}}{9D{\Omega_s}^2 L_r C_r} \tag{8g}$$

The simplified transfer function is a four-order analytical model, which contains one right-half-plane zero w_z and four poles. Where the four poles include a low-frequency pole w_{p1}, a high-frequency pole w_{p2} and a pair of conjugated poles $w_{p3,4}$. The zero-pole map of the simplified model is shown in Fig. 9, and which unites with the frequency response curve of the simplified model is also shown in Fig. 10.

In Fig. 9, the four poles are much closer to imaginary axis by comparing with w_z. Therefore, according to control theory, the influence of the four poles is much larger than w_z. However, w_z is an unstable zero, which may result in an unstable system. Hence, w_z also need to be considered in compensator design process. In Fig. 10, by comparing with switching frequency f_s line, the bandwidth is quite small, thus it should be improved. However, the oscillation peak results from the conjugated poles $w_{p3,4}$ may be larger than 0 dB if the bandwidth increased a lot. Therefore, the conjugated poles $w_{p3,4}$ is also need to be concerned when designing the control loop compensator.

To further investigate the effect factor of these zero and poles, the zero-pole displacement map relates to several key circuit parameters which are switching frequency f_s, duty cycle D, magnetizing inductor L_m, and clamp capacitor C_r are plotted

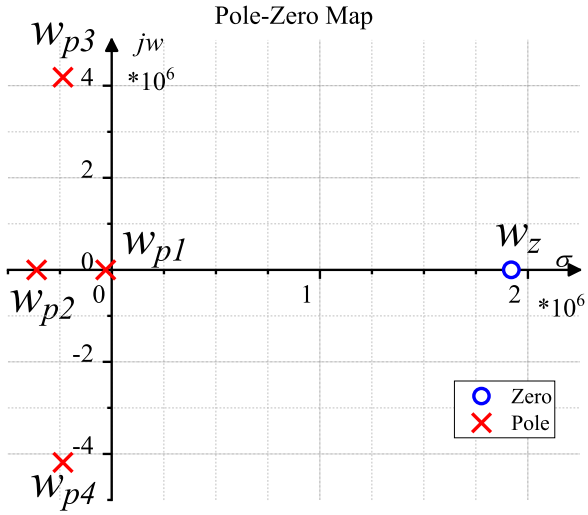

Fig. 9. Poles and zero of the simplified analytical model.

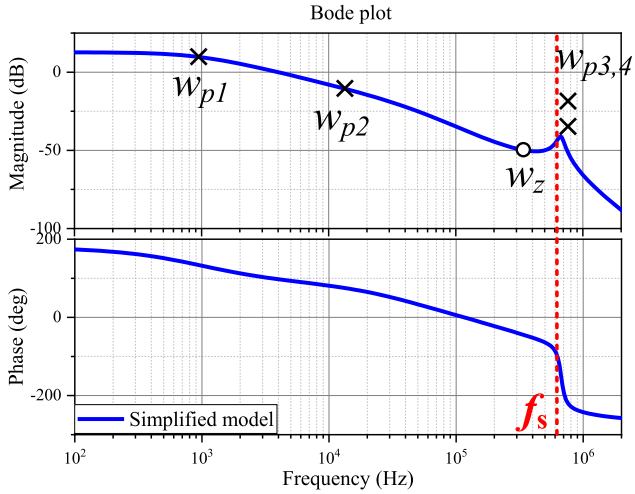

Fig. 10. Frequency response curve of the simplified model in CrCM-ACF converter.

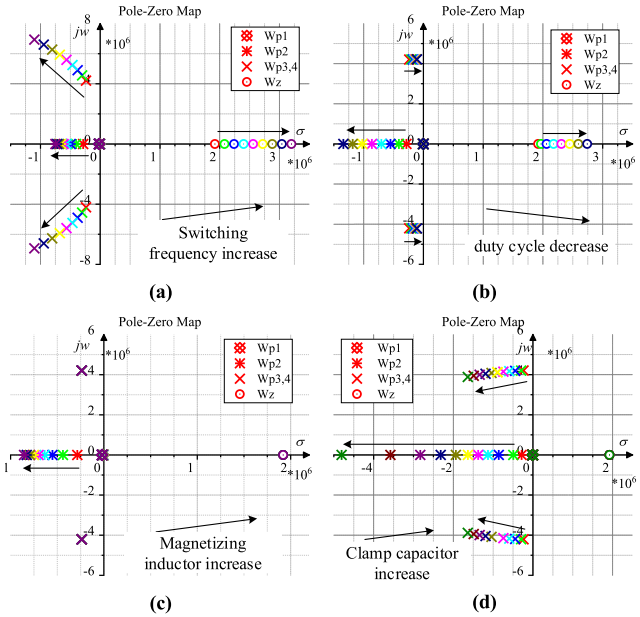

Fig. 11. Zero-pole displacement map when (a) switching frequency, (b) input voltage or duty cycle, (c) magnetizing inductor, and (d) clamp capacitor varies.

in Fig. 11(a) and (b), respectively. In Fig. 11(a), when f_s increases, no obvious variations on w_{p1}, but w_{p2}, $w_{p3,4}$, w_z are all moving away from the imaginary axis. In Fig. 11(b), when D decreases, w_{p1}, w_{p2}, and w_z have the similar shifting principle to f_s increases, but $w_{p3,4}$ are moving closer to the imaginary axis. Note that, D is usually designed below 0.5 in flyback type converter. Hence, Fig. 11(b) is plotted during $D < 0.5$. In Fig. 11(c), only w_{p2} has definite change away from imaginary axis if L_m increases. In Fig. 11(d), if C_r increases, there are no change on w_{p1} and w_z, but there are clear change on w_{p2} and $w_{p3,4}$.

In conclusion, w_{p1} has little variation if these parameter changes, but w_{p2} will be shifted away from the imaginary axis if f_s, L_m, C_r increase or D decreases if $D < 0.5$. The main effect factors of $w_{p3,4}$ are f_s and C_r, $w_{p3,4}$ will be shifted to the negative infinity if f_s and C_r increase. But, there is a small opposite effect when D varies, $w_{p3,4}$ will be shifted closer to the imaginary axis as D decreases if $D < 0.5$. The main effect factors of w_z are f_s and D, w_z will be moved to the positive infinite as f_s increases or D decreases if $D < 0.5$.

IV. Close-Loop Compensator Design

It is very useful and effectively to implement a high performance controller for a high stability and fast dynamic CrCM ACF system. Therefore, a close-loop compensator is designed based on the simplified small signal model, and which will be utilized in a digital controlled CrCM-ACF converter.

The complete control loop of CrCM-ACF converter is shown in Fig. 12. $V_{\rm ref}$ is the reference value of V_o, and V_s is the sampling value of V_o. V_e is the difference between $V_{\rm ref}$ and V_s. $G_{\rm comp}$(s) is the needed compensator. H_d(s) and H_s(s) are the gain of gate driver and sampling resistor network, respectively, and they can be expressed by a constant gain as shown in (9) and (10),

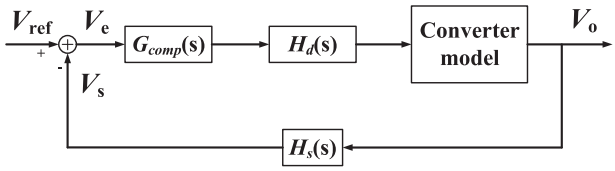

Fig. 12. Total loop model of CrCM-ACF converter in s-domain.

respectively. Therefore, the main part which is applied to design the close-loop compensator is the plant model of CrCM-ACF converter. Based on the simplified control-to-output transfer function $G_{\rm vd\_simp}$(s), the total open-loop transfer function of CrCM-ACF converter is given as (11)

$$H_d(s) = V_{gs} \tag{9}$$

$$H_s(s) = \frac{R_b}{R_a + R_b} \tag{10}$$

$$G_{\rm loop}(s) = G_{\rm vd\_simp}(s) \cdot H_d(s) \cdot G_{\rm comp}(s) \cdot H_s(s) \tag{11}$$

where R_a and R_b are the two resistor, to sense the output voltage.

Empirically, the needed control loop should have a suitable bandwidth, a large low-frequency gain, sufficient phase margin which is around 30–60°, and gain margin which is larger than 10 dB. According to the operating characteristic of CrCM-ACF converter, the minimum switching frequency locates at low input voltage and high load current. Therefore, to obtain a perfect bandwidth, the optimal case to design the controller also should be set at this condition, which is 120 V input voltage and 3.3 A load current in this article. Besides, V_o is 19.5 V, f_s is 600 kHz. The design procedure of the high performance control loop compensator is shown as follows in details.

1) From the frequency response analysis mentioned above, the low-frequency gain is very small, so which should be improved. Hence, an integral unit is needed to increase the low-frequency gain.
2) The cross-frequency of the CrCM-ACF plant model is also small, about 3 kHz at the designed operating conditions. The suitable bandwidth w_c is usually set in the 1/10 to 1/5 of f_s. Therefore, to get a high dynamic CrCM-ACF converter, w_c should be chosen as large as possible. Hence, w_c is set at the 1/5 of f_s, which is around 120 kHz in this article.
3) Generally, there is a "-1" descending slope in middle frequency band to achieve a stable dynamic process. However, the two poles $w_{\rm p1}$ and $w_{\rm p2}$ in the simplified model and the added integral unit form a "-3" descending slope when passing w_c. Therefore, two zeros $w_{\rm cz1}$ and $w_{\rm cz2}$ are needed to increase the descending slope. In this article, $w_{\rm cz1}$ is set at middle of $w_{\rm p1}$ and $w_{\rm p2}$, $w_{\rm cz2}$ is equal to $w_{\rm p2}$.
4) The right-half-plane zero w_z limits the bandwidth and upraises the frequency response cure, so which has a negative effect on the dynamic performance. To eliminate this bad influence, a poles $w_{\rm cp1}$ is set at w_z to counteract the slope-up after w_z.
5) Since the bandwidth is increased, the harmonic peak results from the conjugated poles $w_{\rm cp3,4}$ may be larger than

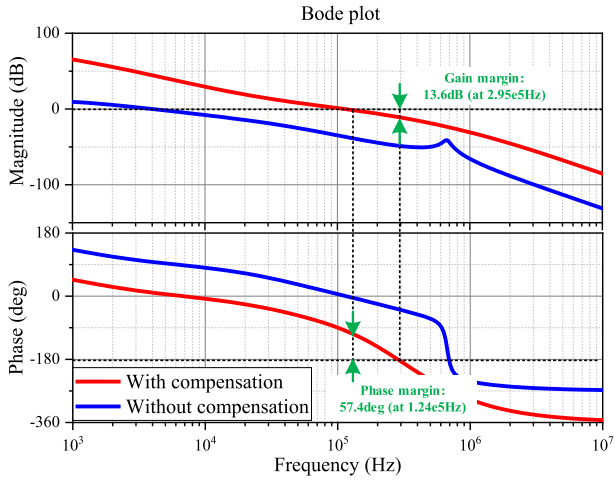

Fig. 13. Frequency response comparison of CrCM-ACF converter with and without compensation.

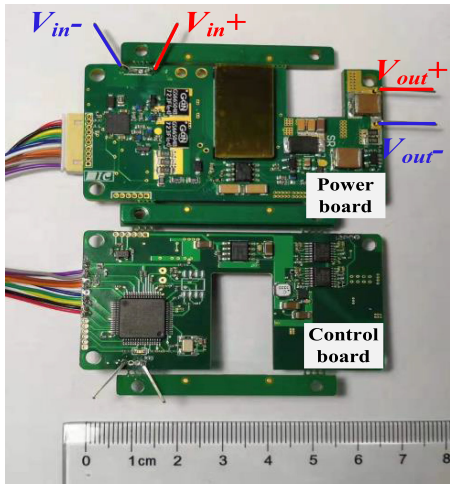

Fig. 14. Photograph of the prototype of CrCM-ACF converter.

0 dB line to perform repeatedly crossing. Therefore, a two-order differentiation element is needed to eliminate this resonance peak. The parameters of this differentiation unit are same to the two-order oscillation elements of $w_{\mathrm{cp3,4}}$ in the simplified model.

6) Moreover, to damping the high-frequency noise of the system, a high-frequency pole w_{cp2} is needed to decrease the high-frequency gain quickly. w_{cp2} is set at the three times of w_z in this article.

According to the above detailed procedure, the designed control loop compensator is given as (12a), the needed poles and zeros in this high performance controller are also given in (12b)–(12g), respectively.

$$G_{\mathrm{comp}}(s) = \frac{K_s(s+w_{\mathrm{cz1}})(s+w_{\mathrm{cz2}})(s^2+as+b)}{s(s+w_{\mathrm{cp1}})(s+w_{\mathrm{cp2}})} \tag{12a}$$

$$w_{\mathrm{cz1}} = \frac{1}{2}(w_{p1}+w_{p2}) \tag{12b}$$

$$w_{\mathrm{cz2}} = w_{p2} \tag{12c}$$

$$a = \frac{9}{4}D{\Omega_s}^3 L_r C_r \tag{12d}$$

$$b = \frac{5}{4}{\Omega_s}^2 \tag{12e}$$

$$w_{\mathrm{cp1}} = w_z \tag{12f}$$

$$w_{\mathrm{cp1}} = 3w_z \tag{12g}$$

where K_s is the dc gain of the designed compensator. $w_{\mathrm{cz}\,1}$ and $w_{\mathrm{cz}\,2}$ are the zeros in the designed compensator, which is set at 5 and 10 kHz, respectively. $w_{\mathrm{cp}\,1}$ and $w_{\mathrm{cp}\,2}$ are the poles in the designed compensator, which is set at 300 and 900 kHz, respectively. a and b are the coefficients of the two-order differential element.

The frequency response comparison of CrCM-ACF converter with and without compensation is shown in Fig. 13. It can be observed that, the bandwidth and low-frequency gain are all improved by using the designed compensator. After compensation, the bandwidth is 124 at a 600 kHz switching frequency. Moreover, the phase margin is 57.4°, and the gain margin is 13.6 dB, which can satisfy the control request. Moreover, there is "−1" descending slope when crossing the bandwidth point, the oscillation peak is eliminated, and the high-frequency gain of the total open-loop is decreased rapidly. Therefore, the proposed compensator can be further applied in CrCM-ACF system.

TABLE II
DESIGN SPECIFICATION

No.	Component	Part	Model / Value
1	Main power switch	S_1	GaN System GS66502B
2	Clamp power switch	S_2	GaN system GS66502B
3	Planar transformer	T_r	Ferroxcube ER23-3F46
4	Output rectifier	S_D	On Semiconductor FSV15100V
5	Gate driver	/	Silicon Laboratories Si8273
6	Micro controller	/	STMicroelectronics STM32F334

V. EXPERIMENTAL RESULTS AND HARDWARE IMPLEMENTATION

A. Frequency Response Verification

To verify the proposed small signal model, a digital controlled CrCM-ACF prototype is designed, as shown in Fig. 14. This CrCM-ACF prototype includes two parts, power, and control board. The ACF topology and gate driver circuit are included in the power board, the sampling and control circuit are built in the control board. The designed specification of this CrCM-ACF prototype is shown in Table II. The designed circuit parameters can refer to Table I in details.

Based on the designed digital CrCM-ACF converter, the primary key waveforms at different load status are shown in Figs. 15 and 16. V_{in} and V_{o} are set at 120 and 19.5 V, respectively, in these two figures. I_o is set at full load current 3.3 A in Fig. 15, while

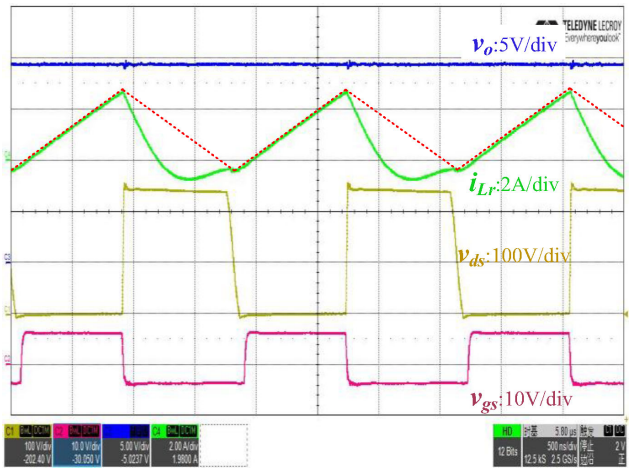

Fig. 15. Primary key waveforms of CrCM-ACF converter at full load.

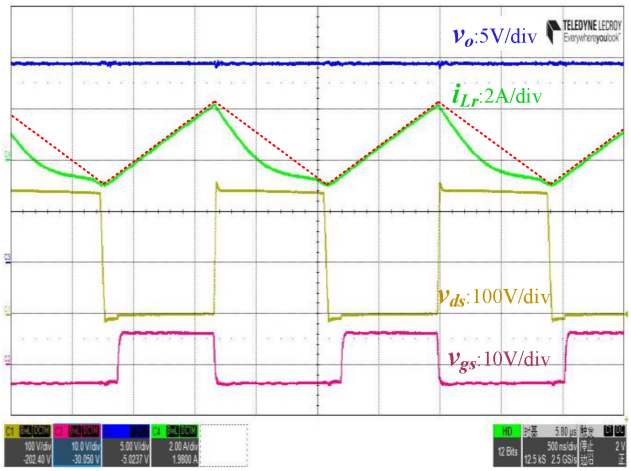

Fig. 16. Primary key waveforms of CrCM-ACF converter at half load.

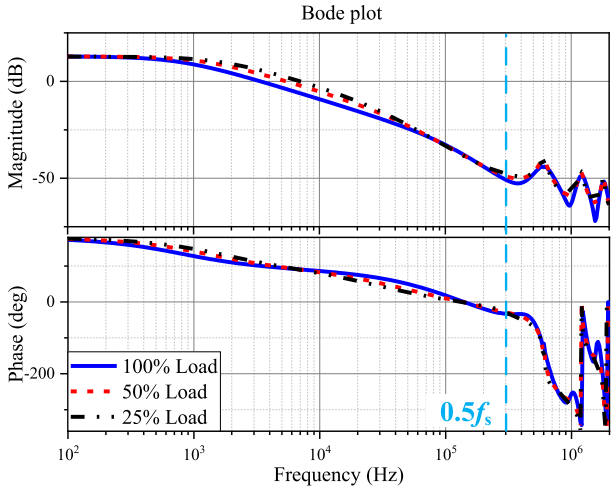

Fig. 17. Frequency response comparison at different load currents.

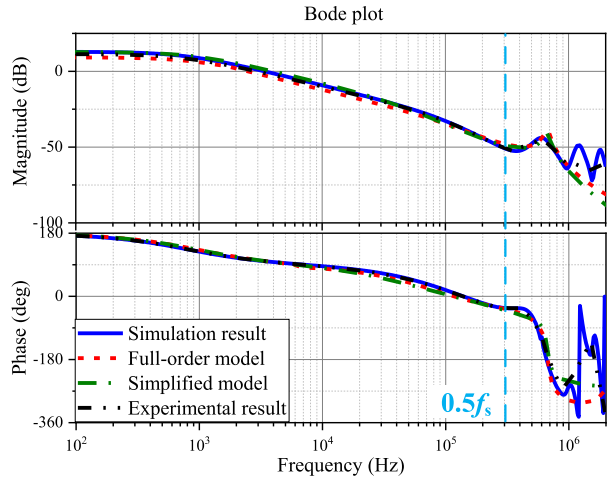

Fig. 18. Frequency response verification when $V_{\rm in} = 120$ V, $I_o = 3$ A, $f_s = 600$ kHz.

it is half load condition 1.67 A in Fig. 16. $i_{\rm Lm}$ is plot as a red dotted line due to it cannot be tested directly by oscilloscope.

In Figs. 15 and 16, the turning point of $V_{\rm ds}$ from high to low also is the end of $M_{\rm b2}$ and the start of $M_{\rm b3}$ in Fig. 2(b). From the tested current waveforms, it can be seen that, $i_{\rm Lr}$ and $i_{\rm Lm}$ have been equaled before this turning point. Moreover, the resonant current waveform is a sinusoidal curve, which is different from the linear resonant current waveform in CCM-ACF converter in [4] and [5]. Therefore, the designed ACF converter is operated in CrCM, and all the energy is transferred to the output side in the resonance process $M_{\rm b2}$. Since I_o is reflected by $i_{\rm Lr}$ and $i_{\rm Lm}$ synchronously, it can be inferred that, S_D can realize ZCS easily at its turnOFF instant.

By using the circuit parameters in Table I, the frequency response curves at different load currents are simulated and presented, as shown in Fig. 17. The load currents are set at 100%, 50%, and 25%, the input and output voltage are set at 120 V and 19.5 V, respectively in this figure. From Figs. 10 and 17, it can be analyzed that the low-frequency pole w_{p1} will become larger and the high-frequency pole w_{p2} will become smaller if the load current increases, but the amplitude of variation is not large. Therefore, the whole frequency response curve has a small variation if the load current changes.

Based on the designed CrCM-ACF prototype, the frequency response curves at different operating status are tested using network analyzer. The simulation results are also presented to verify the accuracy the frequency response of the derived model. Figs. 18–20 show the comparison of the frequency response curves among the derived full-order model, simplified model, simulation results, and measured results of the control-to-output transfer function. In these three figures, the working conditions are selected as low input voltage high load, middle input voltage middle load, and high input voltage light load for representing the wording range of CrCM-ACF converter. Hence, V_o is set at 19.5 V. $V_{\rm in}$ is set at 120, 250, and 380 V, respectively. I_o is set at 3, 2, and 1 A, respectively. In CrCM-ACF converter, in order to realize the ZVS of S_1 and obtain high efficiency, f_s should be changed to regulate I_v [30]. Therefore, f_s is set at 600 kHz, 800 kHz, and 1 MHz, respectively.

In real applications, the useful range of frequency response curve is located at low and middle frequency band, which is

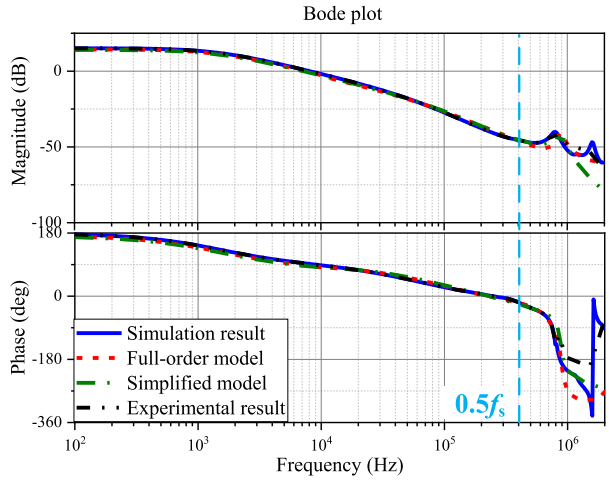

Fig. 19. Frequency response verification when $V_{\rm in} = 250$ V, $I_o = 2$ A, $f_s = 800$ kHz.

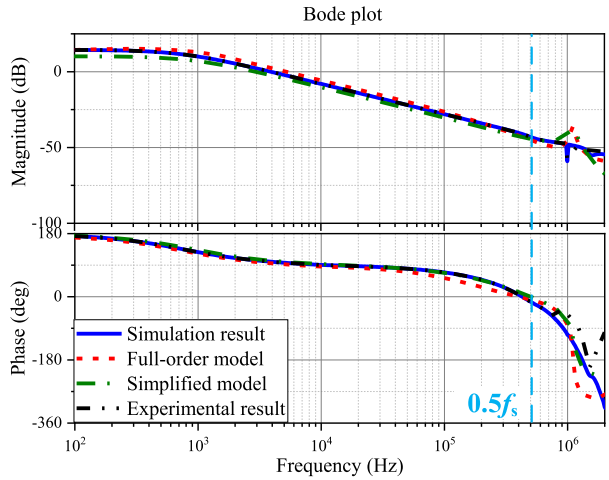

Fig. 20. Frequency response verification when $V_{\rm in} = 380$ V, $I_o = 1$ A, $f_s = 1$ MHz.

usually smaller than the half of switching frequency. From Figs. 18–20, it can be seen that, the proposed full-order analytical model is excellently agreement with the simulation and experimental results except those beyond the half of switching frequency. The discrepancy is because of the side-band effect [2]. It also can be observed that the simplified model, which removes the nonsignificance zeros and poles, are also highly coincident with the simulation and experimental results in the range of the half of switching frequency.

B. Hardware Implementation

To Further verify the practicability of the simplified analytical model and proposed compensator, a digital feedback control loop is implemented, as shown in Fig. 21. From Table II, the adopted digital controller is a microcontroller unit (MCU) STM32F334, which is produced by STMicroelectronics Company. This MCU has integrated the analog-to-digital converter (ADC) and high-resolution timer (HRTIM) module, which also has the programmable logic and optional unit (LOU).

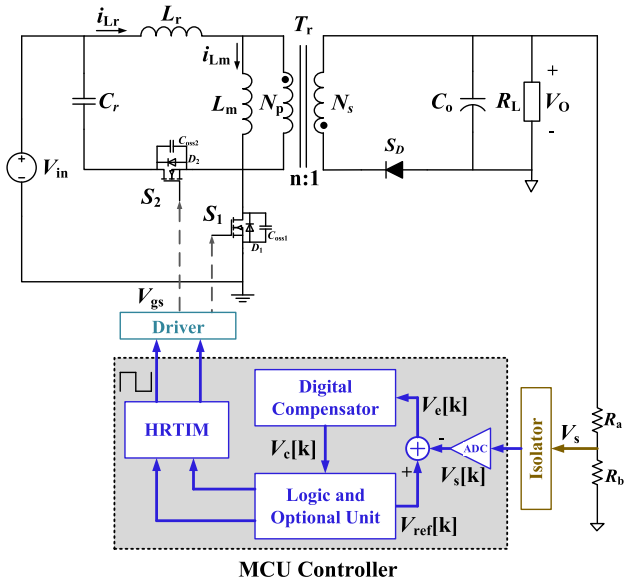

Fig. 21. Adopted digital close-loop control scheme of CrCM-ACF converter.

In Fig. 21, V_s[k] is the sampling value of V_o, $V_{\rm ref}$[k] is the reference value of V_o, V_e[k] is the difference between V_s[k] and $V_{\rm ref}$[k], and V_c[k] is the compensated value of V_e[k]. Using two sampling resistor R_a and R_b and an isolator, V_o is sensed by ADC module, and then V_s[k] is obtained. Perform the operation in (13), V_e[k] is calculated, and then which is compensated to produce V_c[k] by the used digital compensator. The relationship between V_c[k] and V_e[k] is given as (14), where $G_{\rm comp}(z)$ is obtained by transferring the designed *s-domain* compensator $G_{\rm comp}(s)$ into *z-domain*, as shown in (15)

$$V_e[k] = V_{\rm ref}[k] - V_s[k] \tag{13}$$

$$V_c[k] = V_e[k] G_{\rm comp}(z) \tag{14}$$

$$G_{\rm comp}(z) = \frac{K_z(a_0 + a_1 z^{-1} + a_2 z^{-2} + a_3 z^{-3} + a_4 z^{-4})}{b_0 + b_1 z^{-1} + b_2 z^{-2} - b_1 z^{-3} + b_4 z^{-4}} \tag{15a}$$

where

$$K_z = \frac{K_s}{2T_s} \tag{15b}$$

$$a_0 = (T_s^2 b + 2T_s a + 4)(T_s w_{cz1} + 2)(T_s w_{cz2} + 2) \tag{15c}$$

$$a_1 = 4(b w_{cz1} w_{cz2} T_s^4 + ((a w_{cz2} + b) w_{cz1} + b w_{cz2}) T_s^3 - 4(a + w_{cz1} + w_{cz2}) T_s - 16) \tag{15d}$$

$$a_2 = 2(3b w_{cz1} w_{cz2} T_s^4 - 4((a + w_{cz2}) w_{cz1} + a w_{cz2} + b) T_s^2 + 48) \tag{15e}$$

$$a_3 = 4(b w_{cz1} w_{cz2} T_s^4 - ((a w_{cz2} + b) w_{cz1} + b w_{cz2}) T_s^3 + 4(a + w_{cz1} + w_{cz2}) T_s - 16) \tag{15f}$$

$$a_4 = (b T_s^2 - 2a T_s + 4)(T_s w_{cz1} - 2)(T_s w_{cz2} - 2) \tag{15g}$$

$$b_0 = (T_s w_{cp1} + 2)(T_s w_{cp2} + 2) \tag{15h}$$

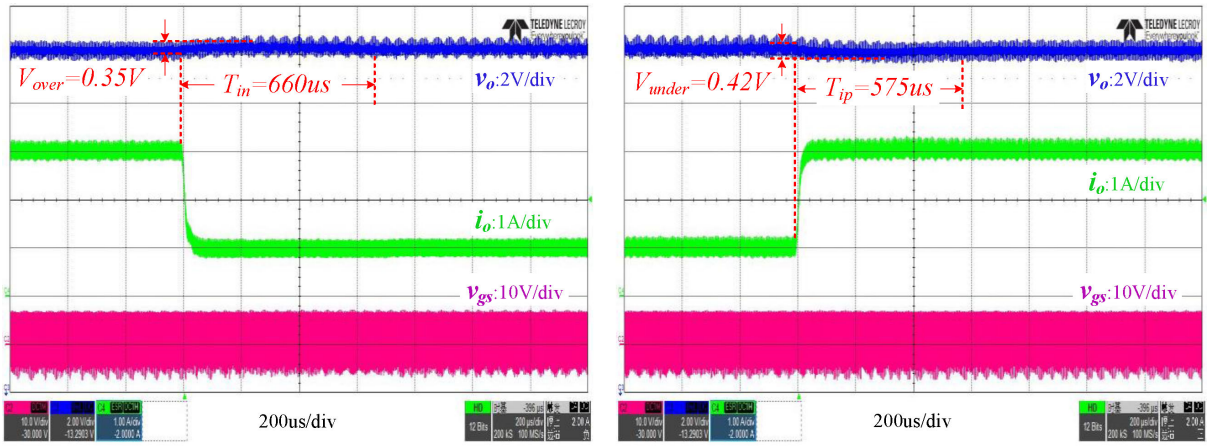

Fig. 22. Dynamic responses during load steps between 3 and 1.5 A. (a) Negative load step from 3 to 1.5 A. (b) Positive load step from 1.5 to 3 A.

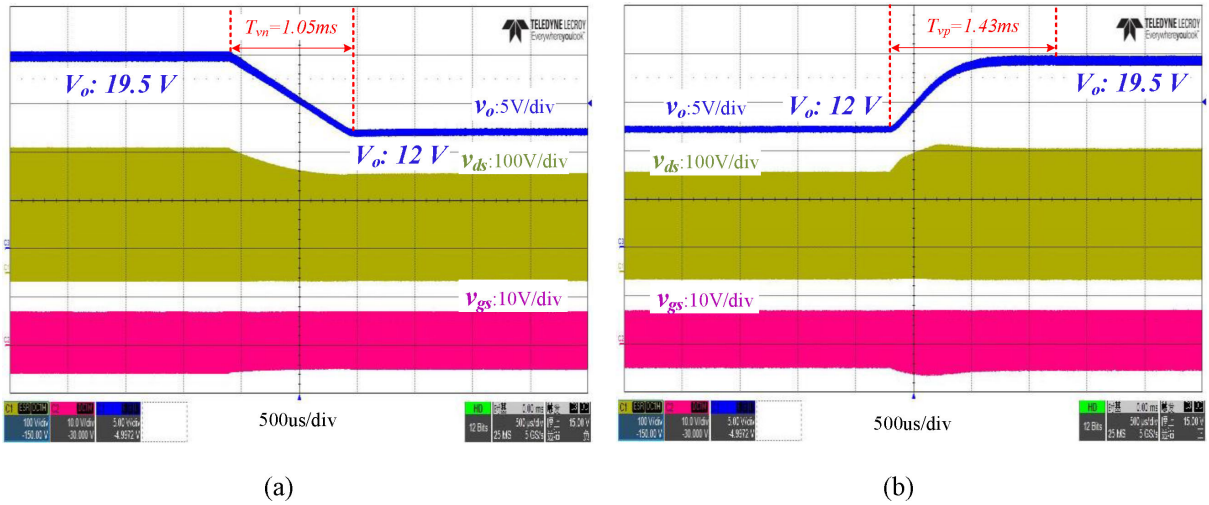

Fig. 23. Dynamic responses when reference voltage steps between 19.5 and 12 V. (a) Negative reference step from 19.5 to 12 V. (b) Positive reference step from 12 to 19.5 V

$$b_1 = 2(T_s^2 w_{cp1} w_{cp2} - 4) \tag{15i}$$

$$b_2 = -4T_s(w_{cp1} + w_{cp2}) \tag{15j}$$

$$b_4 = -(T_s w_{cp1} - 2)(T_s w_{cp2} - 2). \tag{15k}$$

According to the value of V_c[k], D is changed by LOU in every switching cycle. Through HRTIM and gate driver, the relative control signals can be generated to control the turn-ON and turn-OFF states of S_1 and S_2, so V_o can be regulated.

Based on this digital control scheme, the tested dynamic waveforms during negative and positive load steps between high load and middle load are shown in Fig. 22(a) and (b), respectively. V_o is set at 19.5 V, and I_o is varied between 3 and 1.5 A. In Fig. 22(a), when a negative load step occurs from 3 to 1.5 A, the generated voltage overshoot $V_{\rm over}$ is 0.35 V, and the needed regulating time $T_{\rm in}$ is 660 μs. In Fig. 22(b), when a positive load step happens from 1.5 to 3 A, the undershoot voltage $V_{\rm under}$ is 0.42 V, but a smaller regulating time $T_{\rm ip}$ which is 575 μs is needed to stabilize V_o again.

The same to traditional flyback converter, ACF also will be widely used in small power adapters, such as PC and phone chargers, so multioutput voltages will be a common function in ACF converter. Therefore, the dynamic responses during reference voltage steps are also presented to verify the effectiveness of the designed control loop compensator, as shown in Fig. 23(a) and (b). The reference voltage $V_{\rm ref}$ is changed from 19.5 to 12 V and from 12 to 19.5 V, respectively, in these two figures. When $V_{\rm ref}$ has a negative steps from 19.5 to 12 V, a 1.05 ms regulating time $T_{\rm vn}$ is needed to change the output voltage. While, when a positive reference voltage steps from 12 to 19.5 V, the regulating time $T_{\rm vp}$ is 1.43 ms. The simulation results of the corresponding negative and positive reference steps are also given in Fig. 24(a) and (b), respectively. By comparing with the regulating time during reference steps, there is a small difference between the simulation and experimental dynamic responses when using the designed controller.

These parameters when load and reference variations reflect the dynamic performance of CrCM-ACF converter by using the

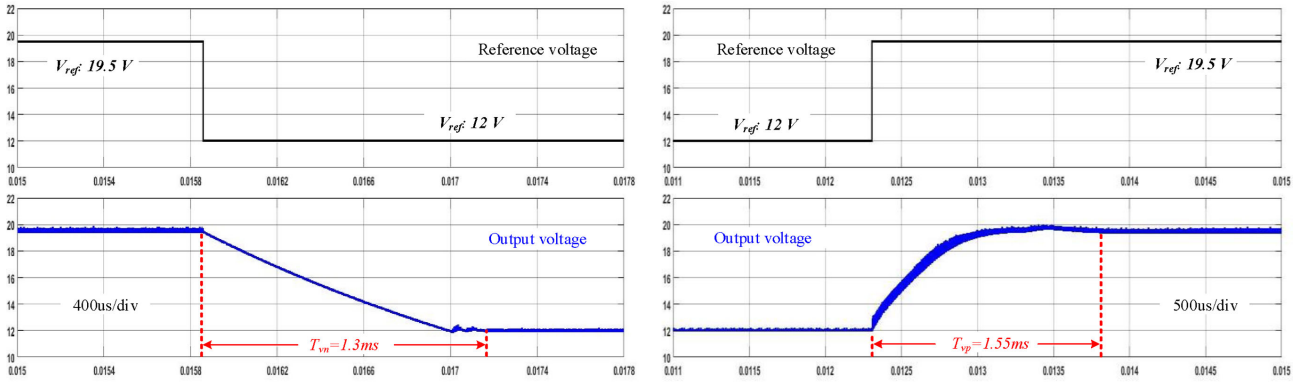

Fig. 24. Simulation of the dynamic responses when reference voltage steps. (a) Negative reference step from 19.5 V to 12 V. (b) Positive reference step from 12 to 19.5 V

implemented close-loop compensator. The tested dynamic performances can meet the requirements if CrCM-ACF converter is adopted in small power supplies. Therefore, the proposed small signal model and designed digital compensator can be well used in CrCM-ACF converter.

VI. Conclusion

An accurate small signal model of CrCM-ACF converter, which is derived by EDF modeling method is proposed in this article. In the modeling process, a zero-input resonant equivalent circuit is used to express the half-PWM half-resonant operating characteristic of CrCM-ACF converter for the first time. Then the full-order analytical model of CrCM-ACF converter is derived using EDF method. For easy to apply, the derived high-order control-to-output transfer function is simplified to a low-order model. To verify the obtained small signal model, the simulation and experimental results are presented based on a 65-W 19.5-V output CrCM-ACF prototype. The comparison results show that the obtained model is highly agreement with the simulation and measurement results. Finally, a high performance compensator is designed by using the simplified model, and which is utilized in CrCM-ACF system. The actual measurement results show that the derived small signal model and designed compensator can be well used in CrCM-ACF converter.

Appendix

The undetermined parameters in the matrix model (7) are given as follows:

$$\Omega_s = 2\pi f_s \tag{16}$$

$$I_{\mathrm{Lms}} = \frac{n(1-D)V_o}{\Omega_s L_m} \tag{17}$$

$$I_{\mathrm{Lmc}} = -\frac{n(1-D)V_o}{\Omega_s L_m} \tag{18}$$

$$V_{\mathrm{Crc}} = \frac{\begin{array}{c} D(D-1)(DT_s - T_m)\Omega_s L_r V_{in} \\ +D^2 L_r V_{in} - nV_o(1-D)(L_m+L_r) \end{array}}{(1-D)(L_m+L_r)({\Omega_s}^2 L_r C_r - 1)} \tag{19}$$

$$I_{\mathrm{Lrs}} = -\Omega_s C_r V_{\mathrm{Crc}} - \frac{V_{in}}{L_m+L_r}\cdot D(DT_s - T_m) \tag{20}$$

$$V_{\mathrm{Crs}} = \frac{\begin{array}{c} D(1-D)(DT_s - T_m)\Omega_s L_r V_{in} + \\ D^2 L_r V_{in} - nV_o(1-D)(L_m+L_r) \end{array}}{(1-D)(L_m+L_r)({\Omega_s}^2 L_r C_r - 1)} \tag{21}$$

$$I_{\mathrm{Lrc}} = -\Omega_s C_r V_{\mathrm{Crs}} + \frac{V_{in}}{L_m+L_r}\cdot D(DT_s - T_m) \tag{22}$$

$$K_s = \frac{I_{\mathrm{Lms}} - I_{\mathrm{Lrs}}}{\sqrt{\left(I_{\mathrm{Lms}} - I_{\mathrm{Lrs}}\right)^2 + \left(I_{\mathrm{Lmc}} - I_{\mathrm{Lrc}}\right)^2}} \tag{23}$$

$$K_c = \frac{I_{\mathrm{Lmc}} - I_{\mathrm{Lrc}}}{\sqrt{\left(I_{\mathrm{Lms}} - I_{\mathrm{Lrs}}\right)^2 + \left(I_{\mathrm{Lmc}} - I_{\mathrm{Lrc}}\right)^2}}. \tag{24}$$

References

[1] S. H. Yang *et al.*, "High accuracy knee voltage detection for primary-side control in flyback battery charger," *IEEE Trans. Circuits Syst. I, Reg. Papers*, vol. 64, no. 4, pp. 1003–1012, Apr. 2017.

[2] C. H. Cheng, C. J. Chen, and S. S. Wang, "Small-signal model of flyback converter in continuous-conduction mode with peak-current control at variable switching frequency," *IEEE Trans. Power Electron.*, vol. 33, no. 5, pp. 4145–4156, Mar. 2018.

[3] X. Huang, J. Feng, W. Du, F. C. Lee, and Q. Li, "Design consideration of MHz active clamp flyback converter with GaN devices for low power adapter application," in *Proc. Rec. IEEE Appl. Power Electron. Conf.*, May 2016, pp. 2334–2341.

[4] B. R. Lin, H. K. Chiang, K. C. Chen, and D. Wang, "Analysis, design and implementation of an active clamp flyback converter," in *Proc. Int. Conf. Power Electron. Drives Syst.*, Nov. 2005, pp. 424–429.

[5] A. Bakkali, P. Alou, J. A. Oliver, and J. A. Cobos, "Average modeling and analysis of Flyback with active clamp topology based on a very simple transformer," in *Proc. IEEE Appl. Power Electron. Conf.*, May 2007, pp. 500–506.

[6] F. Syu *et al.*, "Design and implementation of 1 MHz active-clamped resonant flyback converter," in *Proc. IEEE Ind. Electron. Soc. Conf.*, Oct. 2017, pp. 4438–4442.

[7] R. Perrin, N. Quentin, B. Allard, C. Martin, and M. Ali, "High-temperature GaN active-clamp flyback converter with resonant operation mode," *IEEE J. Emerg. Sel. Top. Power Electron.*, vol. 4, no. 3, pp. 1077–1085, Sep. 2016.

[8] L. Xue and J. Zhang, "Active clamp flyback using GaN power IC for power adapter applications," in *Proc. IEEE Appl. Power Electron. Conf.*, Mar. 2017, pp. 2441–2448.

[9] Texas Instruments, "UCC28780EVM-002: 45W high-density active-clamp flyback AC-DC converter evaluation module using GaN MOSFETs," 2018. [Online]. Available: https://www.ti.com.cn/tool/cn/UCC28780EVM-002?keyMatch=UCC28780EVM-002&tisearch=Search-CN-everything&usecase=GPN

[10] Texas Instruments, "TIDA-01622: 30W/in3, 94% Efficiency, 65W USB Type-C PD AC/DC adapter reference design," 2018. [Online]. Available: https://www.ti.com.cn/tool/cn/TIDA-01622?keyMatch=TIDA-01622&tisearch=Search-CN-everything&usecase=GPN

[11] A. Davoudi, J. Jatskevich, and T. D. Rybel, "Numerical state-space average-value modeling of PWM DC-DC converters operating in DCM and CCM," *IEEE Trans. Power Electron.*, vol. 21, no. 4, pp. 1003–1012, Jul. 2006.

[12] J. Xu and C. Q. Lee, "A unified averaging technique for the modeling of quasi-resonant converters," *IEEE Trans. Power Electron.*, vol. 13, no. 3, pp. 556–563, May 1998.

[13] A. Davoudi and J. Jatskevich, "Realization of parasitics in state-space average-value modeling of PWM DC-DC converters," *IEEE Trans. Power Electron.*, vol. 21, no. 4, pp. 1142–1147, Jul. 2006.

[14] S. Xu, Q. Qian, B. Ren, and Q. Liu, "An accurate small signal modeling and control loop design of active clamp flyback converter," in *Proc. IEEE Energy Convers. Congr. Expo. Asia*, May 2019, pp. 3259–3264.

[15] R. W. Erickson, S. Cuk, and R. D. Middlebrook, "Large-signal modelling and analysis of switching regulators," in *Proc. IEEE Ind. Electron. Soc. Conf.*, Jun. 1982, pp. 240–250.

[16] L. Zhang, Y. Liu, and H. Xin, "Phase-plane analysis of a microgrid under PQ control mode," in *Proc. Int. Conf. Sustain. Power Genera. Supply*, Sep. 2012, pp. 1–5.

[17] M. Veerachary, "Analysis of fourth-order DC-DC converters: A flow graph approach," *IEEE Trans. Ind. Electron.*, vol. 55, no. 1, pp. 133–141, Jan. 2008.

[18] M. Abbasi, A. Afifi, and M. R. A. Pahlavani, "Signal flow graph modeling of a switching converter with single inductor triple output DC-DC structure," *IET Power Electron.*, vol. 11, no. 7, pp. 1195–1204, 2018.

[19] M. E. Elbuluk, G. C. Verghese, and J. G. Kassakian, "Sampled-data modeling and digital control of resonant converters," *IEEE Trans. Power Electron.*, vol. 3, no. 3, pp. 344–354, Jul. 1988.

[20] D. Maksimovic and R. Zane, "Small-signal discrete-time modeling of digitally controlled PWM converters," *IEEE Trans. Power Electron.*, vol. 22, no. 6, pp. 2552–2556, Nov. 2007.

[21] S. Tian, F. C. Lee, and Q. Li, "A simplified equivalent circuit model of series resonant converter," *IEEE Trans. Power Electron.*, vol. 31, no. 5, pp. 3922–3931, May 2016.

[22] H. Li, J. Shang, B. Zhang, X. Zhao, N. Tan, and C. Liu, "Stability analysis with considering the transition interval for PWM DC-DC converters based on describing function method," *IEEE Access*., vol. 6, pp. 48113–48124, Sep. 2018.

[23] Y. Yan, F. C. Lee, and P. Mattavelli, "Analysis and design of average current mode control using a describing-function-based equivalent circuit model," *IEEE Trans. Power Electron.*, vol. 28, no. 10, pp. 4732–4741, Oct. 2013.

[24] C. H. Chang, E. C. Chang, C. A. Cheng, H. L. Cheng, and S. C. Lin, "Small signal modeling of LLC converters based on extended describing function," in *Proc. Int. Conf. Symp. Comp. Consum. Control*., Jun. 2012, pp. 365–368.

[25] A. Tahavorgar and J. E. Quaicoe, "Stability and small-signal analysis of the dual series-resonant DC-DC converter," *IEEE Trans. Power Electron.*, vol. 34, no. 2, pp. 1420–1430, Feb. 2019.

[26] L. A. G. Rodrigrez, C. Deng, J. C. Balda, and A. E. Mejia, "Analysis, modeling and control of an interleaved isolated boost series resonant converter for microinverter applications," in *Proc. IEEE Appl. Power Electron. Conf.*, Mar. 2016, pp. 362–369.

[27] B. Zhang and M. H. Pong, "Dynamic model and small signal analysis based on the extended describing function and Fourier series of a novel AM ZVS direct coupling DC/DC converter," in *Proc. IEEE Power Electron. Spec. Conf.*, Jun. 1997, pp. 447–452.

[28] L. Xue and J. Zhang, "Highly efficient secondary-resonant active clamp flyback converter," *IEEE Trans. Ind. Electron.*, vol. 65, no. 2, pp. 1235–1243, Feb. 2018.

[29] J. Park, J. Fan, and X. Wang, "A sampled-data model for double edge current programmed mode control (DECPM) in high-frequency and wide-range DC–DC converters," *IEEE Trans. Power Electron.*, vol. 25, no. 4, pp. 1023–1033, Apr. 2010.

[30] Texas Instruments. UCC28780: Adaptive Zero Voltage Switching Active-Clamp Flyback Controller. 2017, [Online]. Available: http://www.ti.com/lit/ds/symlink/ucc28780.pdf

Shengyou Xu (Student Member, IEEE) was born in Henan, China, in 1993. He received the B.S. degree in measurement and control technology and instrumentation from Liaoning Technical University, Huludao, China, in 2016. He is currently working toward the Ph.D. degree in electronics engineering from Southeast University, Nanjing, China.

His current research interests include modeling and control technology of high-frequency power conversion.

Qinsong Qian received the Ph.D. degree in electronics engineering from Southeast University, Nanjing, China, in 2012.

In 2012, he joined the School of Electronic Science and Engineering, Southeast University, where he is currently an Associate Professor. His current research interests include power converter design, simulations, and reliability.

Tao Tao received the B.S. degree in electronic engineering, in 2018, from Southeast University, Nanjing, China, where he is currently working toward the M.S. degree in electronic engineering.

He is currently working with the National Engineering Research Center for ASIC. His current research interests include the control and modeling of high-frequency high-efficiency power converters.

Shengli Lu received the Ph.D. degree in information and physics from Nanjing University, Nanjing, China, in 1994.

His current research interests include VLSI and application-specific integrated circuit.

Weifeng Sun (Senior Member, IEEE) received the B.S., M.S., and Ph.D. degrees in the electronic engineering from Southeast University, Nanjing, China, in 2000, 2003, and 2007, respectively.

Since 2006, he has been with the School of Electronic Science and Engineering, Southeast University, where he is currently a Professor. His research interests include new power device design, power ICs, power device modeling, and power systems.